International Journal on Magnetic Particle Imaging
Vol 2, No 2, Article ID 1612001, 6 Pages

Infinite Science Publishing

Research Article

Simultaneous magnetic particle imaging (MPI) and temperature mapping using multi-color MPI

Christian Stehning* · Bernhard Gleich · Jürgen Rahmer

Philips GmbH Innovative Technologies, Research Laboratories, Hamburg, Germany
*Corresponding author, email: christian.stehning@philips.com

Received 14 July 2016; Accepted 7 December 2016; Published online 14 December 2016

Abstract

Magnetic Particle Imaging (MPI) is a novel imaging technique based on the non-linear magnetization response of super-paramagnetic iron oxide nanoparticles (SPIOs). It has previously been shown that beside the spatial particle distribution, information about the particle type, its environment, and the particle temperature can be obtained from the magnetic particle signal. Successful separation of particle types and temperature measurements has been reported in spectroscopic experiments, but a simultaneous mapping of the particle distribution and temperature in a spatially encoded imaging experiment has not been demonstrated. This work presents simultaneous imaging and temperature mapping using a 'multi-color' reconstruction approach.

I. Introduction

Magnetic particle imaging (MPI) is a new medical imaging approach that enables 3D quantitative imaging of magnetic nanoparticle distributions with high temporal and good spatial resolution [1]. In spectroscopic experiments, it was shown that different particle types, their environment and temperature can be separated based on their spectral response [2–4]. This capability potentially enables temperature monitoring in therapeutic hyperthermia [5–7]. However, while a separation of selected particle types [8, 9] and also different viscosities [10, 11] was shown to be feasible in spatially resolved imaging experiments, spatially resolved temperature mapping has not been demonstrated.

Therefore, the purpose of this work is to provide a proof of principle for a simultaneous reconstruction of the spatial particle distribution, and dynamic information about the particle's temperature using a tempered sample and the previously described 'multi-color' reconstruction approach [9].

This may allow for real-time temperature monitoring in image-guided interventions, such as interstitial hyperthermia, following a direct injection of nanoparticles [12–14].

II. Theory

The MPI signals of particles at different temperatures within an imaging volume overlap additively in a signal vector $\boldsymbol{v}$. For particles characterized at two temperatures, T_1 and T_2, the signal vector is determined by the sum of the products between temperature specific system functions $\boldsymbol{G}_{T1}$, $\boldsymbol{G}_{T2}$ and concentration distribution vectors $\boldsymbol{c}_{T1}$, $\boldsymbol{c}_{T2}$. This equation can be rewritten as a matrix $\boldsymbol{G}_c$ of system functions concatenated along the spatial axis, and a concentration vector $\boldsymbol{c}_c$ consisting of the concatenated individual vectors:

$$\begin{aligned} \boldsymbol{v} &= \boldsymbol{G}_{T1} \cdot \boldsymbol{c}_{T1} + \boldsymbol{G}_{T2} \cdot \boldsymbol{c}_{T2} \\ &= [\boldsymbol{G}_{T1} \boldsymbol{G}_{T2}] \cdot \begin{bmatrix} \boldsymbol{c}_{T1} \\ \boldsymbol{c}_{T2} \end{bmatrix} \\ &= \boldsymbol{G}_c \cdot \boldsymbol{c}_c \,. \end{aligned} \tag{1}$$

II.I. Reconstruction of particle concentration

A 3D concentration map can be obtained from the sum of the individual channels:

$$\boldsymbol{c} = \boldsymbol{c}_{T1} + \boldsymbol{c}_{T2} \,. \tag{2}$$

Eq. (2) assumes linear particle characteristics over the present range of concentrations. For very high particle concentrations, e.g. in undiluted Resovist®, the linearity assumption may not hold [15].

II.II. Reconstruction of local temperature information

Ideally, if particles at only the two temperatures $T1$ and $T2$ are present in the imaging volume, separate images (or "channels") $\boldsymbol{c}_{T1}$ and $\boldsymbol{c}_{T2}$ for the two differently tempered particle distributions are obtained by solving the inverse problem for the combined $\boldsymbol{G}_c$ and object vector $\boldsymbol{c}_c$ [9]. However, under realistic conditions, the difference in particle response between two temperatures (as characterized by $\boldsymbol{G}_{T1}$ and $\boldsymbol{G}_{T1}$) is not large enough to achieve full signal separation in the inversion step. Therefore, a fractional signal from particles having temperature T_1 will be present in image $\boldsymbol{c}_{T2}$ and vice versa. Nonetheless, the temperature can be determined: particles at temperature T_1 will have more signal in image $\boldsymbol{c}_{T1}$ than in image $\boldsymbol{c}_{T2}$, whereas particles at temperature T_2 will have more signal in image $\boldsymbol{c}_{T2}$. For intermediate temperatures, the difference between the channels will be smaller. Thus, in a (piecewise) linear approximation in a sufficiently narrow temperature range, a temperature information can be obtained from the difference between the two channels normalized to the particle concentration, which is determined by the sum of the two channels (cf. Eq. (2)):

$$\Delta T(\boldsymbol{r}) \simeq \frac{\boldsymbol{c}_{T1}(\boldsymbol{r}) - \boldsymbol{c}_{T2}(\boldsymbol{r})}{\boldsymbol{c}_{T1}(\boldsymbol{r}) + \boldsymbol{c}_{T2}(\boldsymbol{r})} \,. \tag{3}$$

$\Delta T(\boldsymbol{r})$ represents the spatially resolved temperature offset relative to a reference temperature. For clarity, the dependence on spatial position $\boldsymbol{r}$ is explicitly introduced here. For the sake of brevity, it is referred to as a "temperature map" in the following sections. Due to the unknown particle properties over a wide range of temperatures and concentrations, the linear approximation may be limited to a small temperature range, such as that encountered in an *in vivo* scenario.

III. Methods

III.I. MPI procedure

Imaging was performed using the Philips pre-clinical demonstrator system [16]. The system has selection field gradients of $G_x = G_y = 1.25\,\mathrm{Tm}^{-1}$ and $G_z = 2.50\,\mathrm{Tm}^{-1}$. The resulting field free point (FFP) was driven on a 3D Lissajous trajectory with a repetition time of TR = 21.54 ms by applying drive field frequencies of $f_x = 26.04\,\mathrm{kHz}$, $f_y = 24.51\,\mathrm{kHz}$, and $f_z = 25.25\,\mathrm{kHz}$. A 3D volume was covered by applying amplitudes of 16 mT in all directions, with the FFP covering a $25.6 \times 25.6 \times 12.8\,\mathrm{mm}^3$ volume. Signals were detected using a dedicated three-axis receiver coil, so that the x, y, and z components of the field response were detected simultaneously.

III.II. Calibration procedure

The elements of the concatenated system function $\boldsymbol{G}_c$ needed for image reconstruction were determined on a grid of 28×30×14 voxels of dimensions $1.2 \times 1.2 \times 1.2\,\mathrm{mm}^3$, which covered the extent of the FFP trajectory plus an extra margin to account for the nonideal point spread function [17]. The grid positions were traced using a 3-axis robot cantilever (Isel automation, Eichenzell, Germany). Undiluted Resovist® (Bayer Schering, Germany) was filled into cylindrical cavities (delta probes) that were drilled in small plates of plastic with a diameter of 1 mm and a thickness of 1 mm (0.8 μl of undiluted Resovist®, 22 μg Fe).

Individual system functions $\boldsymbol{G}_{T1}$ and $\boldsymbol{G}_{T2}$ were acquired at room temperature $T_1 = 22$°C, and at $T_2 = 37$°C using the tempering setup described in section III.IV. Signals were averaged over 20 Lissajous cycles of duration TR= 21.54 ms at each position. The calibration procedure yields a $\boldsymbol{G}_c$ matrix for each receiver channel, which describes the spectral response (matrix columns) at each spatial position [9]. A spectral or frequency component represents a spatial pattern (matrix row) that encodes the respective spatial information and temperature information.

III.III. Color MPI image reconstruction

The employed algorithm to reconstruct the multi-color MP images is identical to that described in [10]. The essential reconstruction steps are an SNR-based selection of the spectral MPI signal components, iterative reconstruction with a non-negativity constraint, and a degree of regularization which balances the SNR and spatial resolution based on visual inspection of the images.

III.IV. Phantom setup

A phantom setup with one tempered and one non-tempered sample was assembled as shown in Fig. 1, Fig. 2,

10.18416/ijmpi.2016.1612001

and Fig. 3, respectively. The same samples as described in the calibration procedure were employed. The two samples were mounted on a small plastic hose at a distance of 15 mm.

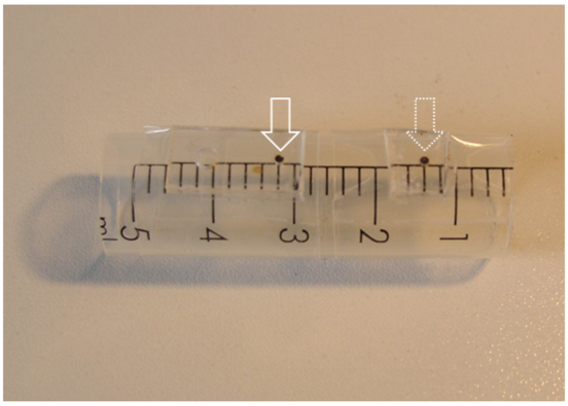

Figure 1: Plastic tube with Resovist samples (arrows).

The two samples were attached to a robot cantilever for positioning near the scanner isocenter. One of the samples was tempered via a looped silicone hose supplied with tempered distilled water.

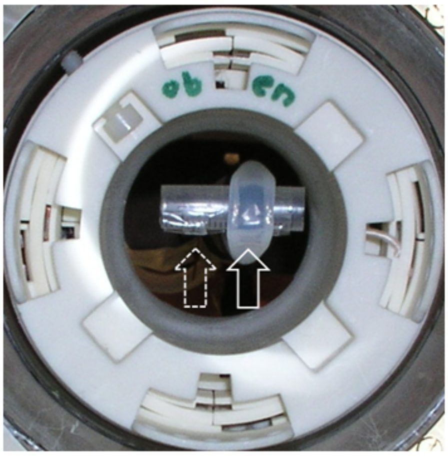

Figure 2: Reference sample (dotted arrow, left) and tempered sample with silicone hose (solid arrow, right) positioned in the scanner bore.

The water was circulated using a flux pump, and tempered using a heat exchanger on a hot plate, as shown in Fig. 3. The circulation temperature was measured using a liquid filled glass thermometer in the water bath.

The reservoir and hose were insulated to reduce loss of heat. The hot plate and flux pump were installed outside of the MPI shielding cabin to avoid interference. The water circulation was heated over a time of 2 hours to reach an equilibrium at $T_W = 37°\text{C}$. 60 seconds after imaging was started, the water reservoir was filled with ice cubes, lowering the water temperature to $T_C = 12°\text{C}$ within a time span of 390 seconds. An MPI signal was continuously acquired during the procedure.

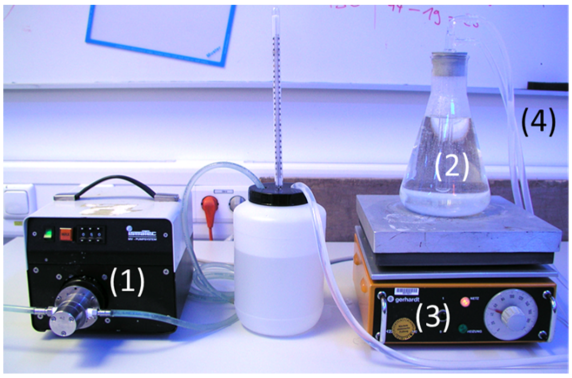

Figure 3: Heating setup. Water is circulated using a flux pump (1) and tempered via a heat exchanger (2) on a hot plate (3). The silicone hoses (4) were insulated to reduce heat loss.

Due to the unknown thermal properties of the silicone hose, the actual thermal transfer rate between the water circulation and probe is unknown. However, if the water circulation temperature is constant over a prolonged period, the probe approaches a temperature plateau approximately equal to the measured temperature in the water bath (equilibrium). Furthermore, the probe temperature is expected to follow a change in the water circulation temperature in an approximately exponential fashion.

IV. Results

The time-resolved signal traces measured in a ROI in the two sample volumes are shown in Fig. 4. The reconstructed particle amount was obtained by integrating the concentration vector of Eq. (2) over a region of interest (ROI) containing the respective sample volume:

$$C = \sum_{\text{ROI}} \boldsymbol{C} = \sum_{\text{ROI}} \boldsymbol{c}_{T1} + \sum_{\text{ROI}} \boldsymbol{c}_{T2}. \tag{4}$$

The time-resolved sample temperature offset ΔT_{ROI} was obtained in an equivalent fashion by integrating the temperature map $\Delta \boldsymbol{T}(\boldsymbol{r})$ of Eq. (3) over the respective sample volume:

$$\Delta T_{\text{ROI}} = \sum_{\text{ROI}} \Delta \boldsymbol{T}(\boldsymbol{r}). \tag{5}$$

For the sake of brevity, ΔT_{ROI} will be referred to as the "sample temperature" T_{REF} and T_{TEMP}, respectively. The signal traces of the reference sample, C_{REF} and T_{REF}, are shown in black, while the signals of the tempered samples, C_{TEMP} and T_{TEMP}, are shown in light gray, respectively.

The particle amount was not calibrated and is plotted in arbitrary units to allow for a visualization within the

10.18416/ijmpi.2016.1612001

same plot as the temperature traces. Two scaling factors were employed, which were different for the particle amount- and temperature signals; identical scaling was performed for the two samples.

Due to the simple setup, which only allows for an independent measurement of the actual probe temperatures at two time points at the beginning and at the end of the experiment, the linearity of the measured signal w.r.t. to the absolute sample temperatures is yet to be confirmed.

Furthermore, the proportionality between signal and concentration has not been determined for our measurement. Therefore, all traces are displayed in arbitrary units.

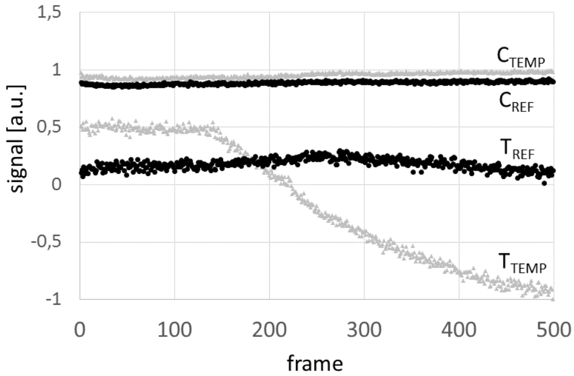

Figure 4: Reconstructed MPI signal traces reflecting the amount of particles (C_{TEMP} and C_{REF}) and temperature information (T_{TEMP} and T_{REF}) of the tempered- and reference probe.

The reconstructed particle amounts C_{REF} and C_{TEMP} of the two samples, as well as the temperature signal of the untempered reference sample, T_{REF}, remain constant over the imaging experiment. Furthermore, the reconstructed particle amounts of both samples with same size were equivalent. The temperature signal of the tempered probe, T_{TEMP}, declines as the circulation temperature is lowered. The temperature-induced signal change amounts to –33% of the signal level in the "warm" channel (not shown) for the here employed temperature range of 25 K.

A more detailed graphical analysis of the dynamic sample temperature T_{TEMP} in the tempered sample is shown in Fig. 5.

The temperature plateaus during the initial phase with constant medium temperature. After lowering the water circulation temperature by adding ice cubes (transient phase), the probe temperature follows in a near-exponential fashion. The two phases are illustrated with linear- and exponential trend lines, respectively (dashed line). Some deviations between the transient signal and a purely exponential decline were observed, which might be attributed to a delayed temperature response of the water circulation after adding ice cubes.

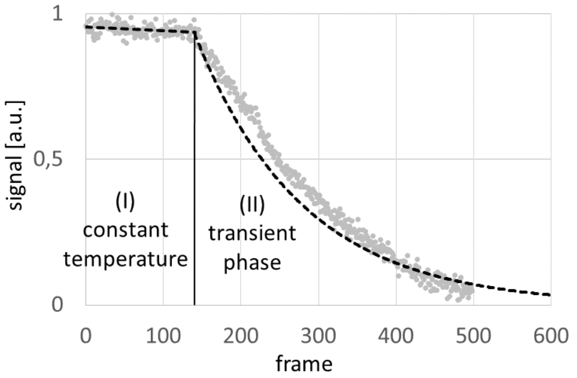

Figure 5: Graphical analysis of the temperature T_{TEMP} obtained in the tempered probe. The dynamic signal may be classified into an equilibrium phase with constant temperature (I), and a transient phase with a near-exponential temperature decline (II). Respective linear- and exponential trend lines are shown for illustration in the same plot (dotted line).

Despite the lack of data for a quantitative analysis, a coarse estimation of the temperature measurement precision can be obtained from an analysis of the signal variation during the equilibrium phase with known temperature (cf. Fig. 5). The standard variation of the temperature signal on the plateau amounts to 0.019 [a.u.], while the signal drop during the subsequent cooling-down phase over a temperature range of $\Delta T = 25\,\mathrm{K}$ amounts to 1.0. In the case of a linear signal behavior in this temperature regime, which is yet to be verified, the ratio of signal variation on the plateau versus the total signal drop suggests a temperature measurement precision of approx. 0.5 K.

For an illustration of spatially resolved imaging and temperature mapping, selected frames depicting a projection image (sum of data along the viewing plane normal) of the time-resolved 3D MPI data are shown in Fig. 6 [a-f], respectively. Early frames acquired at $T_1 = 37$°C are shown in the upper row, while later frames, acquired after the circulation temperature has been lowered to $T_2 = 12$°C, are shown in the bottom row. The "cold channel", $\boldsymbol{c}_{T1}$, is shown in Fig. 6 [a,b], while the "warm channel", $\boldsymbol{c}_{T2}$, is shown in Fig. 6 [c,d]. The color-coded subtraction images Fig. 6 [e,f] represents the temperature map $\Delta\boldsymbol{T}(\boldsymbol{r})$ according to Eq. (3). The color map is scaled to the reference temperatures in the water bath at the beginning and end of the experiment, respectively. The images were smoothed with a small Gaussian convolution kernel for improved visualization, and to cope with a small spatial offset between the two channels.

Spatial maps showing the two delta probes could be reconstructed, and the decreased temperature of the tempered sample (solid arrows, right) is clearly visible in the color-coded temperature map, while no change was observed for the reference sample at room temperature (dotted arrows, left).

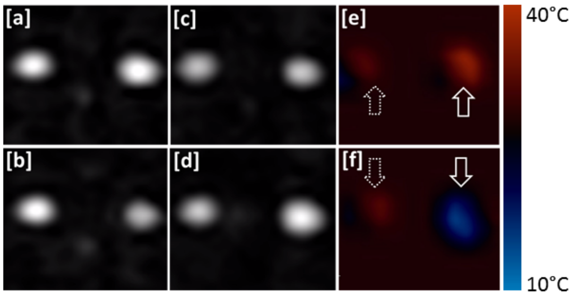

Figure 6: Projection images of 3D reconstructed signal channels [a]-[d], and color-coded difference signal representing temperature [e], [f] acquired at the beginning [top row] and end [bottom row] of the experiment. The images of the delta probes were smoothed with a Gaussian convolution kernel for improved visualization.

V. Discussion and conclusion

The dynamic temperature signal trace of the tempered probe reflects a realistic response to the temperature of the water circulation. The probe temperature T_{TEMP} plateaus during the phase with constant water temperature, and declines as the water circulation temperature was cooled by adding ice cubes.

The signal of the untempered sample, T_{REF}, remained constant over the same imaging period. The reconstructed particle amounts of the two samples, C_{TEMP} and C_{REF}, were stable over the entire imaging experiment, and approximately equal between the two probes with identical dimensions. The estimated precision of the temperature measurement is ±0.5°C for the integrated signal of the delta probes. The temperature maps in Fig. 6 illustrate the feasibility of spatially resolved temperature mapping. The precision is lower in such a spatially resolved experiment when compared to the integrated signal of the entire delta probe, but may be improved by temporal instead of spatial averaging, as signal changes in thermal processes can be expected to be slow compared to the 46 Hz frame rate of the MPI measurement.

Due to the simple experimental setup including a small delta probe covered with a silicone hose, no precise reference temperature, e.g. using a fiberoptic thermometer or infrared camera, could be performed during the transient temperature phase. Instead, the actual sample temperatures were estimated via the water bath at two time points at the beginning and at the end of the experiment only, which currently inhibits the verification of the signal/temperature linearity over the here employed temperature range.

However, these preliminary results provide a proof of principle that a simultaneous spatially resolved reconstruction of particle concentration and temperature information is possible using the previously published color MPI reconstruction technique. Due to its good temporal resolution, dynamic temperature changes can be assesses using the presented approach.

For a more accurate simulation of physiological particle concentrations, lower concentrations of Resovist would need to be employed. This would also avoid potential non-linear effects due to the high particle concentration in undiluted Resovist [15]. Further evaluations should also address *in vivo* situations where the particles are not solved or blood suspended, but bound e.g. in the liver. Furthermore, the mechanisms that yields the temperature-dependent signal change, e.g. alterations of the particle's magnetization slope or hysteresis, could be assessed via measurements or simulations in order to back up the here described experimental results.

Nonetheless, a proof of principle for simultaneous, real-time, 3D spatially resolved temperature and concentration mapping using color MPI has been presented in this work, which, to our knowledge, cannot easily be achieved by other imaging methods.

Acknowledgement

The authors acknowledge funding by the German Federal Ministry of Education and Research (BMBF grant 13GW0069C).

References

[1] B. Gleich and J. Weizenecker. Tomographic imaging using the nonlinear response of magnetic particles. *Nature*, 435(7046):1214–1217, 2005. doi:10.1038/nature03808.

[2] A. M. Rauwerdink, A. J. Giustini, and J. B. Weaver. Simultaneous quantification of multiple magnetic nanoparticles. *Nanotechnology*, 21(45):455101, 2010. doi:10.1088/0957-4484/21/45/455101.

[3] A. M. Rauwerdink and J. B. Weaver. Viscous effects on nanoparticle magnetization harmonics. *J. Magn. Magn. Mater.*, 322(6):609–613, 2010. doi:10.1016/j.jmmm.2009.10.024.

[4] J. B. Weaver, A. M. Rauwerdink, and E. W. Hansen. Magnetic nanoparticle temperature estimation. *Med. Phys.*, 36(5):1822–1829, 2009. doi:10.1118/1.3106342.

[5] T. Kuboyabu, I. Yabata, M. Aoki, N. Banura, K. Nishimoto, A. Mimura, and K. Murase. Magnetic particle imaging for magnetic hyperthermia treatment: Visualization and quantification of the intratumoral distribution and temporal change of magnetic nanoparticles in vivo. *Open J. Med. Imag.*, 6(1):1–15, 2016. doi:10.4236/ojmi.2016.61001.

[6] L. M. Bauer, S. F. Situ, M. A. Griswold, and A. C. S. Samia. High-performance iron oxide nanoparticles for magnetic particle imaging – guided hyperthermia (hmpi). *Nanoscale*, 8(24):12162–12169, 2016. doi:10.1039/C6NR01877G.

[7] K. Murase, M. Aoki, N. Banura, K. Nishimoto, A. Mimura, T. Kuboyabu, and I. Yabata. Usefulness of magnetic particle imaging for predicting the therapeutic effect of magnetic hyperthermia. *Open J. Med. Imag.*, 5(2):85–99, 2015. doi:10.4236/ojmi.2015.52013.

[8] D. Hensley, P. Goodwill, L. Croft, and S. Conolly. Preliminary experimental x-space color mpi. In *International Workshop on Magnetic Particle Imaging (IWMPI)*, 2015. doi:10.1109/IWMPI.2015.7106993.

[9] J. Rahmer, A. Halkola, B. Gleich, I. Schmale, and J. Borgert. First experimental evidence of the feasibility of multi-color magnetic par-

ticle imaging. *Phys. Med. Biol.*, 60(5):1775, 2015. doi:10.1088/0031-9155/60/5/1775.

[10] T. Viereck, C. Kuhlmann, H. Remmer, M. Schilling, and F. Ludwig. Magnetic particle imaging using the viscosity-dependend brownian particle response. In *International Workshop on Magnetic Particle Imaging (IWMPI)*, 2015.

[11] M. Hofmann, J. Dieckhoff, H. Ittrich, and T. Knopp. Experimental distinction of different viscosities using multispectral magnetic particle imaging. In *International Workshop on Magnetic Particle Imaging (IWMPI)*, 2016.

[12] B. Thiesen and A. Jordan. Clinical applications of magnetic nanoparticles for hyperthermia. *Int. J. Hyperthermia*, 24(6):467–474, 2008. doi:10.1080/02656730802104757.

[13] A. Jordan, P. Wurst, H. Fähling, W. John, A. Hinz, and R. Felix. Inductive heating of ferrimagnetic particles and magnetic fluids: physical evaluation of their potential for hyperthermia. *Int. J. Hyperthermia*, 25(7):499–511, 2009. doi:10.3109/02656730903287790.

[14] D. Hensley, P. Goodwill, R. Dhavalikar, Z. W. Tay, B. Zheng, C. Rinaldi, and S. Conolly. Imaging and localized nanoparticle heating with mpi. In *International Workshop on Magnetic Particle Imaging (IWMPI)*, 2016.

[15] N. Löwa, P. Radon, O. Kosch, and F. Wiekhorst. Concentration dependent mpi tracer performance. *International Journal on Magnetic Particle Imaging*, 2(1):1601001, 2016. doi:10.18416/ijmpi.2016.1601001.

[16] B. Gleich, J. Weizenecker, H. Timminger, C. Bontus, I. Schmale, J. Rahmer, J. Schmidt, J. Kanzenbach, and J. Borgert. Fast mpi demonstrator with enlarged field of view. In *Proceedings of the International Society for Magnetic Resonance in Medicine*, volume 18, page 218, 2010.

[17] A. Weber, F. Werner, J. Weizenecker, T. M. Buzug, and T. Knopp. Artifact free reconstruction with the system matrix approach by overscanning the field-free-point trajectory in magnetic particle imaging. *Phys. Med. Biol.*, 61(2):475–487, 2016. doi:10.1088/0031-9155/61/2/475.